ADVANCES IN ATMOSPHERIC SCIENCES, VOL. 40, MARCH 2023, 410–427

• **Original Paper** •

Seasonal Prediction of the Record-Breaking Northward Shift of the Western Pacific Subtropical High in July 2021※

Shuai HU[1], Tianjun ZHOU[*1,2], Bo WU[1], and Xiaolong CHEN[1]

[1]*State Key Laboratory of Numerical Modeling for Atmospheric Sciences and Geophysical Fluid Dynamics, Institute of Atmospheric Physics, Chinese Academy of Sciences, Beijing* 100029, *China*

[2]*University of the Chinese Academy of Sciences, Beijing* 100049, *China*

(Received 8 June 2022; revised 26 September 2022; accepted 17 October 2022)

ABSTRACT

The unprecedented Zhengzhou heavy rainfall in July 2021 occurred under the background of a northward shift of the western Pacific subtropical high (WPSH). Although the occurrence of this extreme event could not be captured by seasonal predictions, a skillful prediction of the WPSH variation might have warned us of the increased probability of extreme weather events in Central and Northern China. However, the mechanism for the WPSH variation in July 2021 and its seasonal predictability are still unknown. Here, the observed northward shift of the WPSH in July 2021 is shown to correspond to a meridional dipole pattern of the 850-hPa geopotential height to the east of China, the amplitude of which became the strongest since 1979. The meridional dipole pattern is two nodes of the Pacific–Japan pattern. To investigate the predictability of the WPSH variation, a 21-member ensemble of seasonal predictions initiated from the end of June 2021 was conducted. The predictable and unpredictable components of the meridional dipole pattern were identified from the ensemble simulations. Its predictable component is driven by positive precipitation anomalies over the tropical western Pacific. The positive precipitation anomalies are caused by positive horizonal advection of the mean moist enthalpy by southwesterly anomalies to the northwestern flank of anticyclonic anomalies excited by the existing La Niña, which is skillfully predicted by the model. The leading mode of the unpredictable component is associated with the atmospheric internal intraseasonal oscillations, which are not initialized in the simulations. The relative contributions of the predictable and unpredictable components to the observed northward shift of the WPSH at 850 hPa are 28.0% and 72.0%, respectively.

Key words: western pacific subtropical high, seasonal prediction, seasonal predictability, La Niña, Pacific–Japan pattern

Citation: Hu, S., T.-J. Zhou, B. Wu, and X. L. Chen, 2023: Seasonal prediction of the record-breaking northward shift of the western Pacific subtropical high in July 2021. *Adv. Atmos. Sci.*, **40**(3), 410–427, https://doi.org/10.1007/s00376-022-2151-x.

Article Highlights:

- Northward shift of low-level component of the western Pacific subtropical high (WPSH) in July 2021 broke the record held since 1979.
- Predictable and unpredictable components of the WPSH variation in 2021 were identified based on the seasonal prediction from IAP-DecPreS.
- The predictable and unpredictable components are driven by the existing La Niña and atmospheric internal variability, respectively.

1. Introduction

During 19–21 July 2021, an unprecedented heavy rainfall event caused wrenching scenes of devastation in Zhengzhou of Henan Province, which is an inland city in the middle of China. The formation and maintenance mechanisms of this extreme precipitation event have attracted widespread attention (Yang et al., 2021; Zhang et al., 2021, 2022; Cheng et al., 2022; Liang et al., 2022; Nie and Sun, 2022). The event was listed as one of top climate extremes to occur in China in 2021 that deserve further research (Zhou et al., 2022). Understanding the mechanism and predictability of this extreme event, including its possibility of re-occurrence in

※ This paper is a contribution to the special collection on the July 2021 Zhengzhou, Henan Extreme Rainfall Event.

* Corresponding author: Tianjun ZHOU
Email: zhoutj@lasg.iap.ac.cn

the future, has been the research foci of both the weather forecast and climate research communities.

One of the key large-scale background circulation anomalies associated with the Zhengzhou extreme rainfall in July 2021 is the northward shift of the western Pacific subtropical high (WPSH), which is a semi-permanent anticyclonic circulation system in the western north Pacific (Tao and Chen, 1987) and serves as one of the primary components of the East Asian summer monsoon (Wu and Zhou, 2008; Xiang et al., 2013). On the one hand, the southeasterlies at the west flank of the northward extended WPSH enhance the westward moisture transportation in cooperation with tropical Typhoon "In-Fa" (2021). On the other hand, the WPSH inhibits the eastward-moving low vortex over Henan Province during the extreme rainfall event. Both processes are favorable for the extremely rapid accumulation of water vapor on the regional scale (Zhou et al., 2022).

The Pacific–Japan (PJ) pattern, also referred to as the East Asia–Pacific pattern (EAP), is one of the most important teleconnections modulating the WPSH and East Asian summer climate (Nitta, 1987; Huang and Sun, 1992). The PJ pattern is characterized by the correlation relationship between the convective activity near the Philippine Sea and the rainfall over midlatitude East Asia. When enhanced (suppressed) convective activity near the Philippine Sea is observed, anticyclonic (cyclonic) anomalies tend to arise over the midlatitude Far East (the western North Pacific) (Kosaka and Nakamura, 2006, 2010). The PJ pattern can be regarded as a dynamical mode excited in the zonally asymmetric baroclinic basic flow over East Asia with an efficient self-sustaining mechanism through moist processes (Kosaka and Nakamura, 2006). The PJ pattern includes broadband temporal variability on the intraseasonal, interannual, and interdecadal time scales (Kubota et al., 2016; Wu et al., 2016; Tao et al., 2017; Xu et al., 2019; Sun et al., 2021). On the interannual time scale, the PJ pattern is closely related to El Niño–Southern Oscillation (ENSO), the Indian Ocean basin wide warming, and regional air–sea interaction in the tropical western north Pacific (Chen and Zhou, 2014; Tao et al., 2017). On the intraseasonal time scale, the convective heating associated with the Madden–Julian Oscillation (MJO), the boreal summer intraseasonal oscillation (BSISO), typhoon activity, and the Rossby wave breaking in the exit region of the Asian jet can excite the PJ pattern (Yamada and Kawamura, 2007; Wang et al., 2016; Takemura and Mukougawa, 2020; Ling and Lu, 2022).

Understanding the formation mechanism of the northward shift of the WPSH in July 2021 is crucial for accurate climate predictions, but up to now, rarely has any investigation focused on the predictability of the abnormal WPSH in July 2021. The main motivation of this study is to address the following three scientific questions: (1) Why does the WPSH shift north in July 2021? (2) Can we predict the northward shift of the WPSH? (3) What are the sources and restrictions of the predictability?

2. Model, data, and method

2.1. *Model and experiment design*

In this study, we used the seasonal to decadal climate prediction system IAP-DecPreS, which was developed by the State Key Laboratory of Numerical Modeling for Atmospheric Sciences and Geophysical Fluid Dynamics (LASG) in the Institute of Atmospheric Physics (IAP) of the Chinese Academy of Sciences (CAS) (Wu et al., 2015, 2018; Hu et al., 2019, 2020).

The IAP-DecPreS is composed of two parts, the coupled climate system models FGOLAS-f3-L, and the weakly coupled data initialization scheme EnOI-IAU (Wu et al., 2018). The FGOLAS-f3-L is one of three versions of the CAS model that have participated in the Coupled Model Intercomparison Project Phase 6 (CMIP6) (Zhou et al., 2020). The atmospheric component of FGOALS-f3-L is FAMIL (Zhou et al., 2015; Li et al., 2019), which is established on a finite volume dynamical core on a cubed-sphere grid with the horizontal resolution approximately equal to 1°×1°. The FAMIL has 32 layers in the vertical direction, with the top layer at 2.16 hPa (Guo et al., 2020a; He et al., 2020b). The oceanic component of FGOALS-f3-L is the low-resolution LICOM3 (Yu et al., 2018; Lin et al., 2020), which has 360 grid cells in the zonal direction and 218 grid cells in the meridional direction approximately equal to 1°×1°. To better resolve the equatorial waves, the meridional resolution refines from 1° to 0.5° near the equator. The low-resolution LICOM3 has 30 layers in the vertical direction, which is 10 m per layer in the upper 150 m and divided in uneven vertical layers below 150 m.

The FGOLAS-f3-L can reasonably reproduce the upper-level South Asian High, the low-level monsoonal circulations, the WPSH, and the mid-Pacific trough, and thus simulate the observed climatological vertical shear of meridional winds in July over the tropical western Pacific (Fig. 1). As mentioned in previous studies, the vertical shear of the climatological-mean meridional winds is vital for the baroclinic energy conversion from the basic flow to the perturbations associated with the PJ pattern (Kosaka and Nakamura, 2006). More details about the FGOALS-f3-L can be found in He et al. (2020a); Guo et al. (2020b); Guo et al. (2020a); He et al. (2020b). The EnOI-IAU assimilates the gridded SST from the HadISST version 1.1 (Rayner et al., 2003) and the subsurface temperature and salinity profiles from the EN4 dataset produced by the Hadley Centre (Good et al., 2013), which form the initial conditions for the FGOLAS-f3-L to conduct climate predictions.

To investigate the predictability of the large-scale circulation anomalies over East Asia in July 2021, 21-member 3-month ensemble seasonal forecast runs were conducted from the end of June in 2021, with initial conditions derived

from the outputs of the three initialization runs based on the EnOI-IAU. The time lagged method was utilized to generate the 21 prediction members. Here, seven start dates from 24 to 30 June were selected. We also used 3-member seasonal hindcast experiments for the period 2000–20 to remove the lead-time dependent model drifts, following the procedures recommended by Boer et al. (2016). The 3-month hindcast runs initialized from the end of June were conducted once per year for the period of 2000–20. More details of the experiment designs can be found in Table 1.

2.2. *Observational data*

In this study, we used monthly and hourly data from the European Centre for Medium-Range Weather Forecasts reanalysis ERA5 with a horizontal resolution of 0.25°×0.25° (Hersbach et al., 2020). We also used the monthly sea surface temperature (SST) data derived from the HadISST version 1.1 at a horizontal resolution of 1°×1° (Rayner et al., 2003). All the datasets cover the period 1979–2021.

2.3. *Analytical method*

To understand the processes responsible for the precipitation anomalies over the tropical western Pacific, we diagnosed the atmospheric moisture equation (Seager et al., 2010; Seager et al., 2012; Chou et al., 2013) as follows:

$$P' = E' - <\bar{\boldsymbol{V}}\cdot\nabla_h q'> - <\bar{\omega}\cdot\partial_p q'> - <\boldsymbol{V}'\cdot\nabla_h\bar{q}> - <\omega'\cdot\partial_p\bar{q}> + \mathrm{NL} + \mathrm{Residual}\,, \tag{1}$$

where P is precipitation, q is specific humidity, $\boldsymbol{V}$ is horizontal wind, ω is vertical pressure velocity, and p represents the vertical direction. The angle bracket $< >$ denotes the mass-weighted vertical integral through the entire atmospheric column. The overbars (primes) represent the climatological monthly mean (monthly anomaly). The horizontal and vertical moisture advection terms can be divided into the thermodynamic components ($- <\bar{\boldsymbol{V}}\cdot\nabla_h q'> - <\bar{\omega}\cdot\partial_p q'>$), the dynamic components ($- <\boldsymbol{V}'\cdot\nabla_h\bar{q}> - <\omega'\cdot\partial_p\bar{q}>$), and the nonlinear components (NL). The "Residual" denotes the residual term.

To estimate the relative contributions of high- and low-frequency eddies to the precipitation anomalies at the monthly time scale, we also used the daily data to diagnose the column-integrated atmospheric moisture equation at intraseasonal (10–30 days) and synoptic (<10 days) timescales. Equation (1) can be rewritten as:

$$\begin{aligned} P' =& \widetilde{E^*} - <\bar{\boldsymbol{V}}\cdot\widetilde{\nabla_h q^*}> - <\bar{\omega}\cdot\widetilde{\partial_p q^*}> - <\boldsymbol{V}^*\cdot\widetilde{\nabla_h\bar{q}}> - <\omega^*\cdot\widetilde{\partial_p\bar{q}}> + \\ & \widetilde{E''} - <\bar{\boldsymbol{V}}\cdot\widetilde{\nabla_h q''}> - <\bar{\omega}\cdot\widetilde{\partial_v q''}> - <\boldsymbol{V}''\cdot\widetilde{\nabla_h\bar{q}}> - <\omega''\cdot\widetilde{\partial_p\bar{q}}> - \\ & <\boldsymbol{V}^*\cdot\widetilde{\nabla_h q''}> - <\omega^*\cdot\widetilde{\partial_p q''}> - <\boldsymbol{V}''\cdot\widetilde{\nabla_h q^*}> - <\omega''\cdot\widetilde{\partial_p q^*}> - \\ & <\boldsymbol{V}''\cdot\widetilde{\nabla_h q''}> - <\omega''\cdot\widetilde{\partial_p q''}> - <\boldsymbol{V}''\cdot\widetilde{\nabla_h q''}> - <\omega''\cdot\widetilde{\partial_p q''}> + \\ & \mathrm{Residual}\,, \end{aligned} \tag{2}$$

where the tilde represents the monthly mean. The superscript $*$ represents the intraseasonal (10–30 days) time scale, and the superscript $''$ represents the synoptic (<10 days) time scale. The intraseasonal and synoptic variations of each variable are obtained by the Lanczos filter. On the right hand side of the equation, the first (second) row is the relative contribution from the intraseasonal (synoptic) variability to the monthly precipitation anomalies. The third and fourth rows are contributions from the interactions between intraseasonal and synoptic variations and synoptic transient processes to the monthly precipitation anomalies, respectively, the sum of which are treated as the nonlinear components.

The atmospheric moist static energy (MSE) equation (Neelin and Held, 1987; Wu et al., 2017) was diagnosed to investigate the processes driving the anomalous vertical motions, which is written as follows:

$$\partial_t <C_pT + L_vq>' + <u\partial_x\left(C_pT + L_vq\right)>' + <v\partial_y\left(C_pT + L_vq\right)>' + <\omega\partial_p h>' = F'_{\mathrm{net}}\,, \tag{3}$$

where C_p and L_v are the specific heat at constant pressure and the latent heat of vaporization. T denotes the air temperature. q is the specific humidity. φ denotes the geopotential. u, v, and ω represent the zonal wind, meridional wind, and vertical pressure velocity, respectively, and x, y, and p represent the zonal, meridional, and vertical direction, respectively. $C_pT + L_vq$ is the atmospheric moist enthalpy, and h denotes the MSE, which is equal to $C_pT + L_vq + \varphi$. F_{net} represents the net flux into the atmospheric column. The primes

Table 1. Designs of seasonal climate prediction experiments.

Exp name	Integration	Ensemble size	Initial condition
Initialization	Jan 1950 to Dec 2021	3	Model states in 1 Jan 1950 from three historical runs
Hindcast	Initiated from the end of each month in each year during 2000–20, integrated 16 months	3	Model states in 25th, 28th, 30th of each month in each year derived from 3 initialization runs
Forecast	Initiated from the end of June in 2021, integrated 3 months	21	Model states in 24–30 June 2021 derived from 3 initialization runs

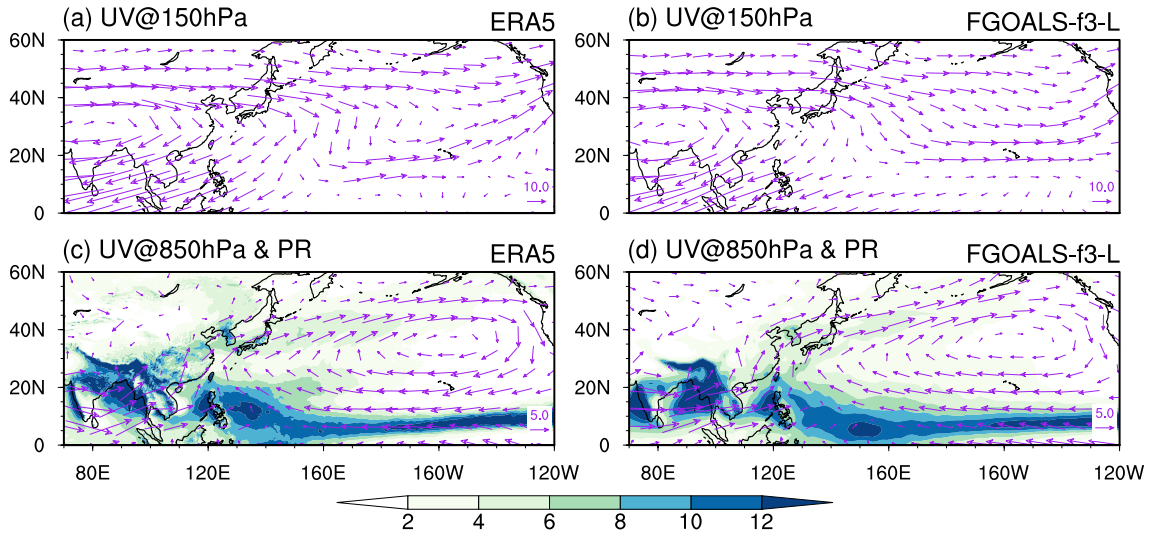

Fig. 1. Left panel: Observed climatological July mean (a) horizontal winds at the 150-hPa level (vectors, units: m s^{-1}) and (c) precipitation (shaded, units: mm d^{-1}) and horizontal winds at the 850-hPa level (vectors, units: m s^{-1}) for the period 1995–2014. The observation derives from ERA5. Right panel: (b, d) as in (a, c), but for the FGOALS-f3-L historical simulations.

represent the monthly anomaly. The angle brackets denote the mass-weighted vertical integral through the entire atmospheric column. The MSE equation can be simplified to

$$\begin{aligned} <\omega'\partial_p\bar{h}> \approx & F'_{\text{net}} - <u'\partial_x\overline{\left(C_pT+L_vq\right)}> - \\ & <\bar{u}\partial_x\left(C_pT+L_vq\right)'> - v'\partial_y\overline{\left(C_pT+L_vq\right)}> - \\ & <\bar{v}\partial_y\left(C_pT+L_vq\right)'> - <\bar{\omega}\partial_p h'> + \text{NL}\,, \end{aligned} \tag{4}$$

where NL is the nonlinear term. The bars (primes) represent the climatological monthly mean (monthly anomaly).

The anomalous net flux into the atmospheric column (F'_{net}) can be written as:

$$F'_{\text{net}} = R'_{\text{cloud}} + R'_{\text{clear}} + S' + \text{LH}' + \text{SH}'\,, \tag{5}$$

where S' represents the net shortwave radiative flux anomalies into the atmospheric column from the surface and the top of atmosphere. The net longwave radiative flux anomalies into the atmospheric column from the surface and the top of atmosphere can be separated into clear-sky and cloud-related components (R'_{clear} and R'_{cloud}). LH′ represents the latent heat anomalies, and SH′ represents the sensible heat anomalies.

The 3D wave-activity flux calculated in this study parallels that of Takaya and Nakamura (2001). The PJ pattern in July is defined as the leading singular vector decomposition (SVD) mode for the 500-hPa geopotential height field over East Asia (10°–70°N, 100°–160°E) and precipitation over the Philippines (10°–30°N, 125°–155°E), following Tao et al. (2017). Before the SVD analysis, both the precipitation anomalies and the 500-hPa geopotential height (Z500) anomalies are standardized and weighted by the square root of cosine of latitudes. SVD analysis also has been used in previous studies to define the PJ pattern at daily time scales (Sun et al., 2021).

Following Boer et al. (2018), the predictable variabilities in the forecast are estimated as the ensemble mean, while the unpredictable or "noise" components are the deviations of each member to the ensemble mean (ensemble spread), which are assumed to be independent among the ensemble members and to average to zero for a sufficiently large ensemble. In this study, we conducted the empirical orthogonal function (EOF) analysis to the ensemble spread to derive the leading modes of the unpredictable variabilities. To measure the intensity of the northward shift of the WPSH, we defined the Z850 dipole index, which is calculated based on the difference of geopotential height anomaly averaged over the low latitudes (20°–35°N, 110°–150°E) and midlatitudes (40°–55°N, 120°–160°E) of the East Asian coastal region. The precipitation anomalies averaged over the western tropical Pacific (15°–30°N, 125°–155°E) is defined as the WP–PR index. The Niño-3.4 index is the area-averaged SSTAs in 5°S–5°N, 170°–120°W. The student's *t* test was used to estimate the significance of regression and correlation analysis.

3. Observational analyses

In July 2021, the most prominent atmospheric circulation anomalies over East Asia were the meridional dipole pattern of geopotential height anomalies at both upper and lower levels, with positive geopotential height anomalies over the North Pacific surrounding the Japan Sea and negative anomalies around the Philippine Sea, respectively (Figs. 2a, b). The anticyclonic anomalies over the midlatitudes show an equivalent barotropic structure and exhibit a zonally elongated shape throughout nearly the whole North Pacific. In contrast, the cyclonic anomalies over the low-latitudes Philippine Sea are confined in the lower level. The year-by-year out-

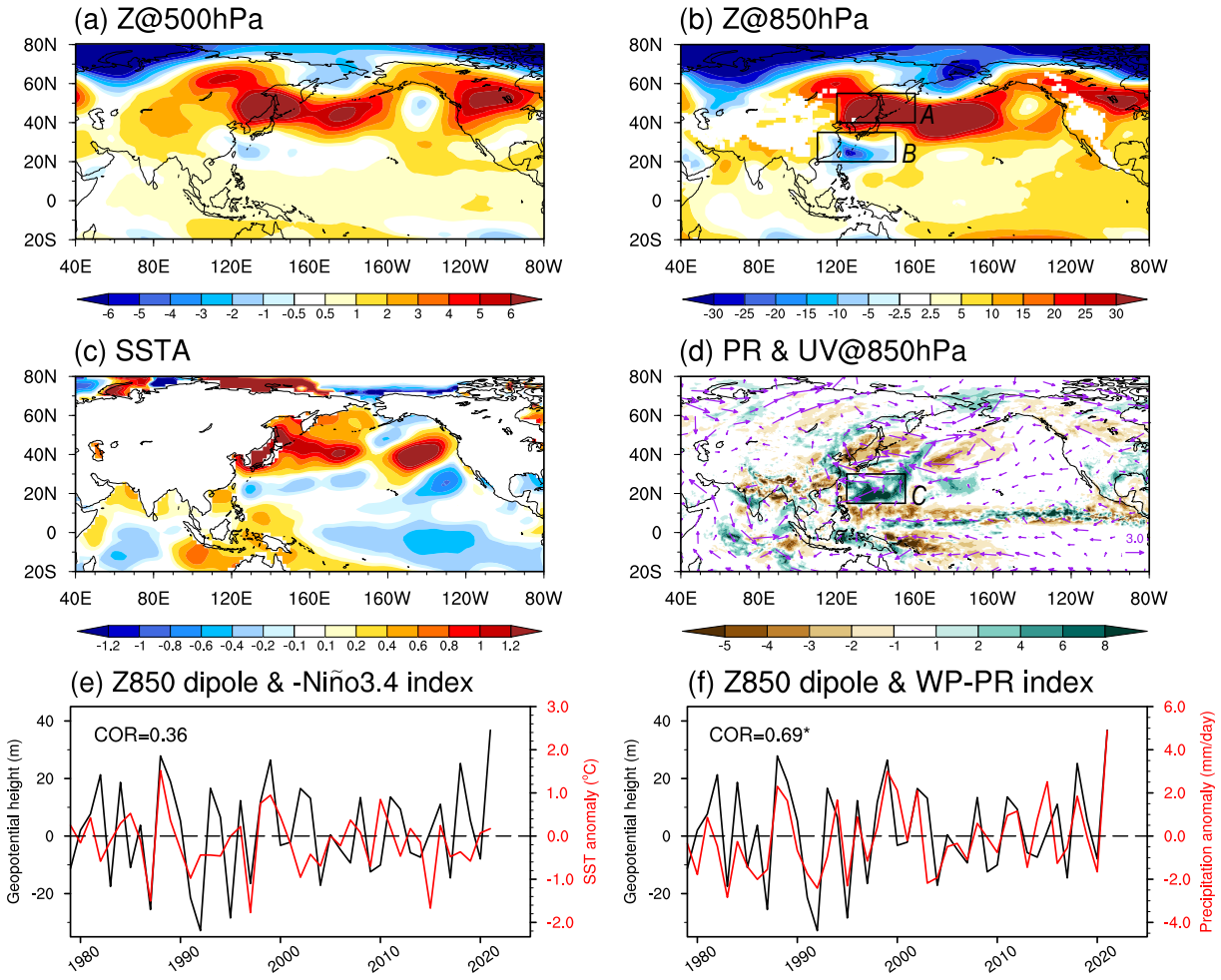

Fig. 2. Spatial distributions of (a) geopotential height anomaly at 500 hPa (units: gpm), (b) geopotential height anomaly at 850 hPa (units: gpm), (c) SSTA (units: °C), and (d) precipitation anomaly (units: mm d^{-1}) and 850-hPa horizontal wind anomaly (units: m s^{-1}) in July 2021. Time series of (e) the July Z850 dipole index and the Niño-3.4 index (the Niño-3.4 index is multiplied by –1), and (f) the July Z850 dipole index and the area-averaged precipitation anomalies over the western tropical Pacific (WP-PR index) for the period 1979–2021. Correlation coefficients between the two indices (COR) are noted at the top left of (e, f), with the asterisk (*) representing significance at the 99% level. The Z850 dipole index is defined as the difference of geopotential height anomaly averaged over Box-A (15°–30°N, 110°–150°E) and Box-B (35°–50°N, 120°–160°E) in (b). The WP-PR index is defined as the precipitation anomalies averaged over Box-C (15°–30°N, 125°–155°E) in (d).

lines of the WPSH in July at 850 hPa, 700 hPa, 600 hPa, and 500 hPa for the period 1979–2021 are shown in Fig. 3. Consistent with the geopotential height anomalies, the tropical component of the WPSH in 2021 is weakened and shifted eastward, while the northward shift of the subtropical component is the strongest since the year 1979. In addition, the northward shift of the WPSH in 2021 is more prominent in the low levels. These circulation anomalies indicate that the WPSH shifts northward in July 2021, and the northward shift in the 850-hPa level breaks the record held since the year 1979. To measure the intensity of the northward shift of the WPSH, we calculated the difference of the 850-hPa geopotential height anomalies between the low latitudes and midlatitudes (the Z850 dipole index hereafter), which is shown as the black line in Fig. 2e. It is evident that the northward shift of the WPSH in July 2021 is the strongest since the year 1979, with the value reaching 36.8 gpm.

Why is there such an extreme northward shift of the WPSH in July 2021? The underlying SSTAs have the same sign as the abnormal meridional dipole circulation pattern, with warm (cold) SSTAs underneath the anticyclonic (cyclonic) anomalies, implying that these SSTAs were driven by the local atmospheric forcings. Midsummer of 2021 experiences the decaying and secondary reinforcing stage of the La Niña event of the preceding winter (https://origin.cpc.ncep.noaa.gov/), and thus, there are La Niña-type negative SSTAs in the tropical central to eastern Pacific (Fig. 2c). Does the concurrent La Niña sufficiently explain the northward shift of the WPSH in July 2021? We examined the relationship between the July Niño-3.4 index and the Z850 dipole index for the period 1979–2021 (Fig. 2e). Although the correlation coefficient between the two

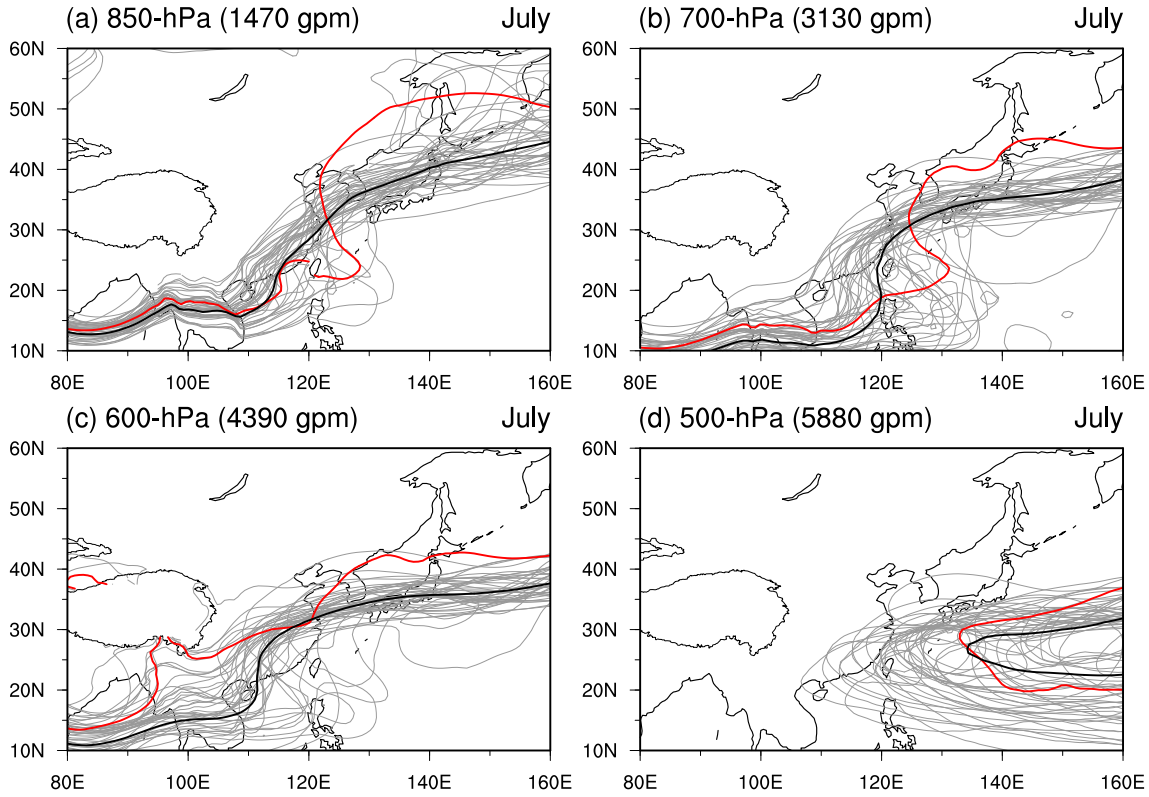

Fig. 3. The western Pacific subtropical high (WPSH) at (a) 850 hPa, (b) 700 hPa, (c) 600 hPa, and (d) 500 hPa in July. The WPSH at 850 hPa, 700 hPa, 600 hPa, and 500 hPa are denoted by the 1470-, 3130-, 4390- and 5880-gpm contour of geopotential height, respectively. The bold black lines represent the climatology for the period of 1979–2021. The red and light gray lines represent the cases in 2021 and other years, respectively.

indices reaches –0.36 (significant at the 95% level), the July Niño-3.4 index in 2021 is not as extreme as the Z850 dipole index, and thus, the La Niña event only partly contributes to the northward shift of the WPSH and cannot fully explain its total intensity. The anomalous cyclone over the Philippine Sea can be explained well by the enhanced convective activity in terms of the Gill model (Gill, 1980) (Fig. 2d), and the anomalous anticyclone over the midlatitude Far East is reminiscent of the response of the PJ pattern, which also has a close relationship with the abnormal convective activity in the Philippine Sea. We found that the convective activity over the western tropical Pacific explains the interannual variability of the Z850 dipole index well, with the correlation coefficient reaching 0.69 (significant at the 99% level), and the extremely strengthened precipitation over the western tropical Pacific in July 2021 is in accord with the variability of the Z850 dipole index (Fig. 2f).

The significant correlation between the meridional atmospheric dipole pattern and the tropical convection indicates the contribution of the PJ pattern. Given that the PJ pattern manifests itself as a quasi-stationary Rossby wave train in the lower troposphere emanating from tropical convection near the Philippines, here we used the SVD analysis to extract the PJ pattern. The first SVD modes for the 500-hPa geopotential height field over East Asia (10°–70°N, 100°–160°E) and precipitation over the Philippine Sea (10°–30°N, 125°–155°E) are shown in Figs. 4a and b and explain 65.2% of the total squared covariance. The homogeneous map of 500-hPa geopotential height anomalies associated with the first SVD mode shows a meridional dipole pattern over East Asia, featuring a typical PJ pattern (Fig. 4a), which is closely related to the convective heating over the Philippine Sea (Fig. 4b). The correlation coefficient between the two expansion coefficients of the first SVD modes is 0.82 (significant at the 99% level). The standardized expansion coefficients of the first SVD indicate that the enhanced convective activity excited a strong PJ pattern in July 2021 (Fig. 4c).

The specific characteristics of the PJ pattern in July 2021 are shown in Fig. 5. The upper-level circulation anomalies are shifted meridionally relative to the low-level anomalies by about a quarter wavelength, with an apparent poleward phase tilt with height. The Rossby waves propagate northward in the lower troposphere and southeastward in the upper troposphere (Fig. 5a), consistent with the idea that the PJ pattern is a superposition of the barotropic and baroclinic modes (Kosaka and Nakamura, 2006, 2010). As seen from the meridional section, the PJ pattern in July 2021 reached downstream to North America through the eastward propagation of stationary Rossby waves (Fig. 5b), which is also consistent with the results of previous studies (Kosaka and Nakamura, 2006; Zhu and Li, 2016, 2018; Sun et al., 2021). The eastward propagation of the stationary Rossby waves resembles the second mode of the teleconnection linking summertime precipita-

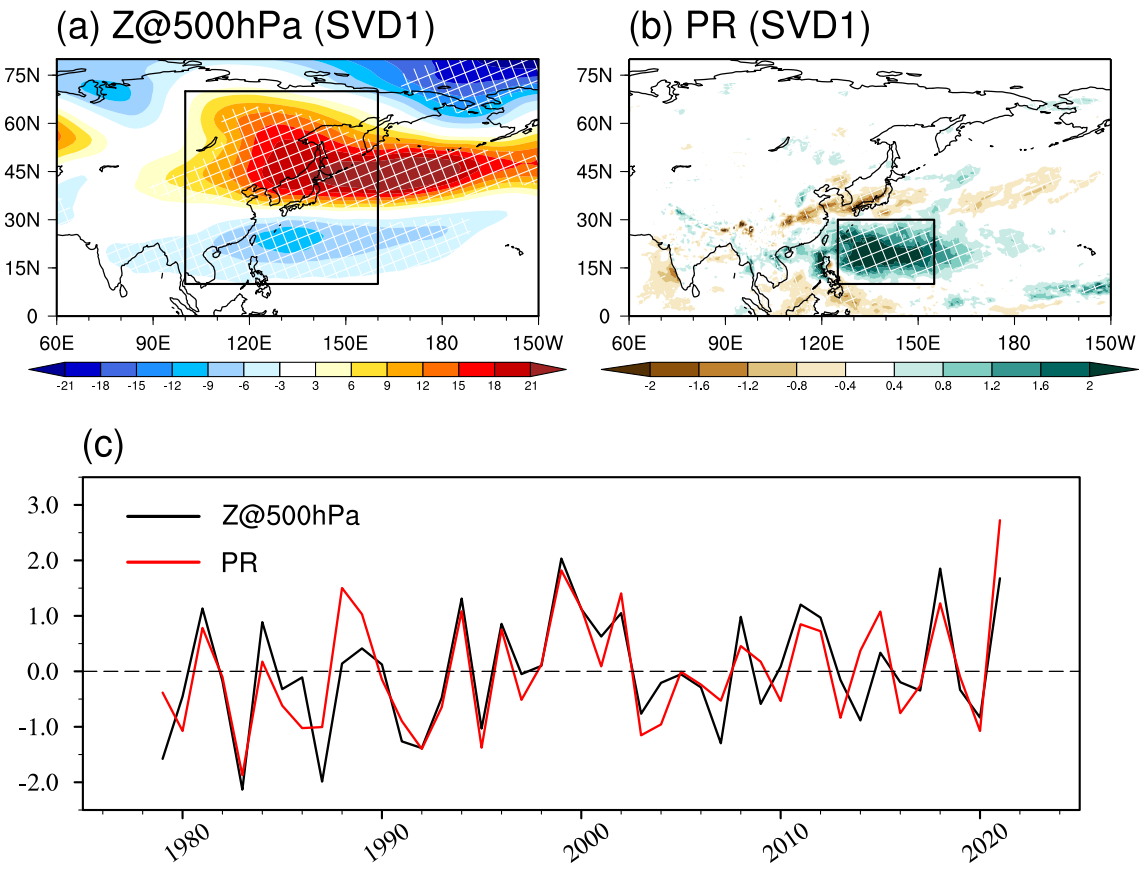

Fig. 4. Spatial distributions of (a) the 500-hPa geopotential height anomalies (units: gpm) and (b) precipitation anomalies (units: mm d^{-1}) associated with the first SVD mode between the July 500-hPa geopotential height field over East Asia (10°–70°N, 100°–160°E) and July precipitation over the Philippines (10°–30°N, 125°–155°E). The hatching denotes values exceeding the 95% confidence level. (c) The expansion coefficients of the first SVD mode. The black (red) line is for the 500-hPa geopotential height (precipitation).

tion variability over East Asia and North America proposed by Lau and Weng (2002), which possibly stems from Rossby wave dispersion from fluctuations of large-scale heat sources. The PJ pattern in July 2021 moved northward by about 10 degrees as compared with the normal condition.

The above analysis shows that the large-scale atmospheric circulation anomalies associated with the Zhengzhou extreme rainfall in July 2021 are results of the northward shift of the WPSH, the amplitude of which is the strongest since 1979. The circulation anomalies are closely linked with the enhanced convective activity over the Philippine Sea, which influences the WPSH via exciting the PJ pattern. So, can we predict the northward shift of the WPSH in July 2021? We address this issue in the next section.

4. Ensemble seasonal forecast

To investigate the predictability of the northward shift of the WPSH in July 2021, we conducted 21-member 3-month ensemble seasonal forecasts initialized from the end of June in 2021 based on the IAP-DecPreS, which assimilates the observed oceanic data (including the SST and subsurface temperature and salinity profiles). The most important source of seasonal predictability stems from the oceanic variation, and thus, we first investigate the prediction of SSTA in July 2021 (Fig. 6). The forecasts from individual ensemble members are in agreement with each other and can predict the observed spatial distribution of SSTA well, with the uncentered pattern correlation coefficient (PCC) between the forecast and the observation ranging from 0.32 to 0.62. Compared with forecasts from individual members, the ensemble mean forecast has the highest prediction skill of PCC, and it reasonably reproduces the observed negative SSTA in the tropical central to eastern Pacific and positive SSTA in the eastern tropical Indian Ocean, the North Pacific, and the tropical South Atlantic (Fig. 6).

In contrast, predictions of the 850-hPa atmospheric circulation over the Northern Hemisphere show spread among the ensemble members (Fig. 7). The prediction skill of individual members for this feature is lower than the prediction skill for the SSTA, with PCCs in 18 out of 21 members below 0.3 (Table 2). The ensemble mean, which is usually regarded as the predictable component in the forecasts, exhibits positive 850-hPa geopotential height anomalies over the midlatitude Far East, suggesting that the northward shift of the WPSH in July 2021 stems at least partly from

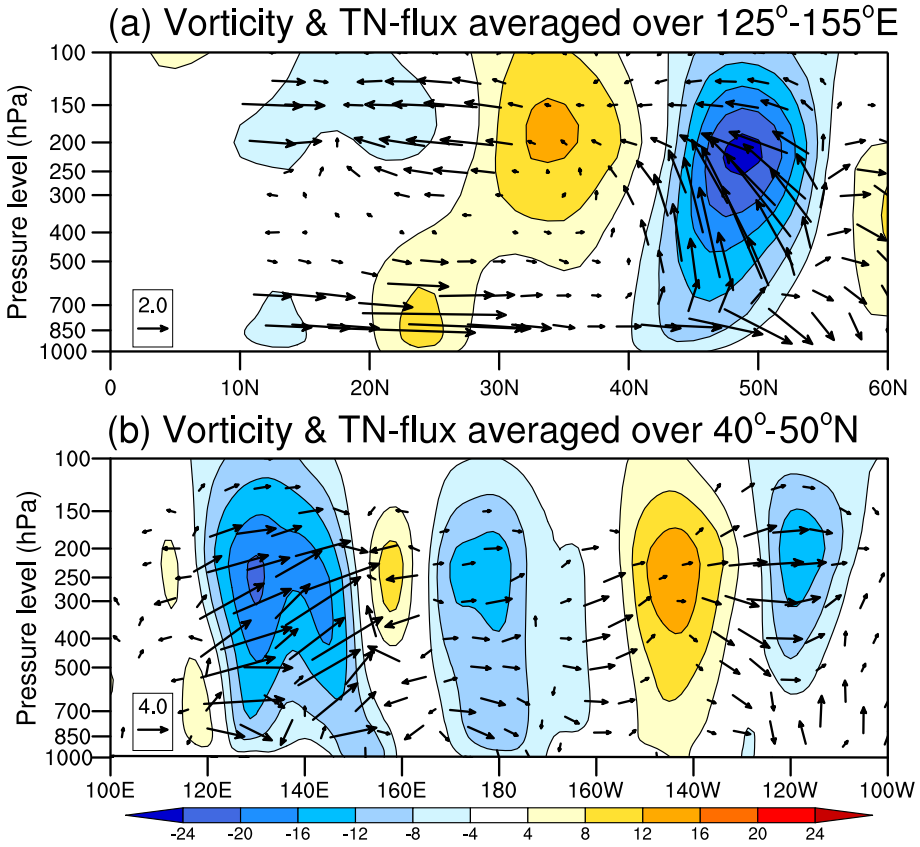

Fig. 5. Relative vorticity anomalies (shaded, units: 10^{-6} s^{-1}) for (a) the meridional sections averaged between 125°–155°E and (b) the zonal sections averaged between 40°–50°N. The 3D TN wave activity fluxes are shown by vectors (units: m^2 s^{-2}), where the vertical components have been multiplied by 100.

the predictable component induced by the initial oceanic conditions. There are two realizations (#21 and #16) matching the observations closely, with PCC reaching 0.70 and 0.54, respectively, indicating that the unpredictable or "noise" component also plays a vital role. Hence, we focus on the respective impacts of the predictable and the unpredictable components of the northward shift of the WPSH in the following sections.

4.1. *Predictable variability*

Figure 8 shows the predictable variability of the large-scale circulation and precipitation anomalies in July 2021, which are derived from the 21-member ensemble mean of the forecasts by IAP-DecPreS. There are positive geopotential height anomalies over northeastern East Asia at both the 500-hPa and 850-hPa levels (Figs. 8a, b), suggesting that part of the variability of the WPSH in July 2021 is predictable, and the IAP-DecPreS can predict the northward shift of the WPSH at a 1-month lead. The predictability stems from the positive precipitation anomalies over the South China Sea and the tropical western Pacific, which excite a PJ pattern with cyclonic (anticyclonic) anomalies over the South China Sea and the tropical western Pacific (northeastern East Asia), respectively (Fig. 8c). The relative vorticity anomalies with a poleward phase tilt with height and the northward propagation of the Rossby waves are consistent with the observations. The prediction shows a northward propagation of Rossby waves in the upper troposphere, instead of the observed southeastward propagation (Figs. 5a and 8d). The predictable PJ pattern is confined over the coastal regions of East Asia, and the intensity of the northward shift of the WPSH is weaker than that seen in the observations. The predicted Z850 dipole index in the ensemble mean prediction is 10.3 gpm, which is about 28.0% of the observed value.

What is the mechanism of the predictable signal? We diagnosed the moisture equation [Eq. (1)] to the precipitation anomalies over the tropical western Pacific (10°–25°N, 125°–150°E). The results show that the positive precipitation anomalies are caused by the positive anomalous advection of the climatological vertical moisture by ascending anomalies ($-<\omega' \cdot \partial_p \bar{q}>$) (Fig. 9a). In the tropical regions with deep convection, the gross moist stability is usually positive and the $\partial_p \bar{h}$ is usually less than 0 (Back and Bretherton, 2006), and thus, the positive terms on the right-hand side of Eq. (4) can drive anomalous ascending motion to keep the MSE budget balance (Biasutti et al., 2018). MSE budget analysis over the tropical western Pacific (10°–25°N, 125°–

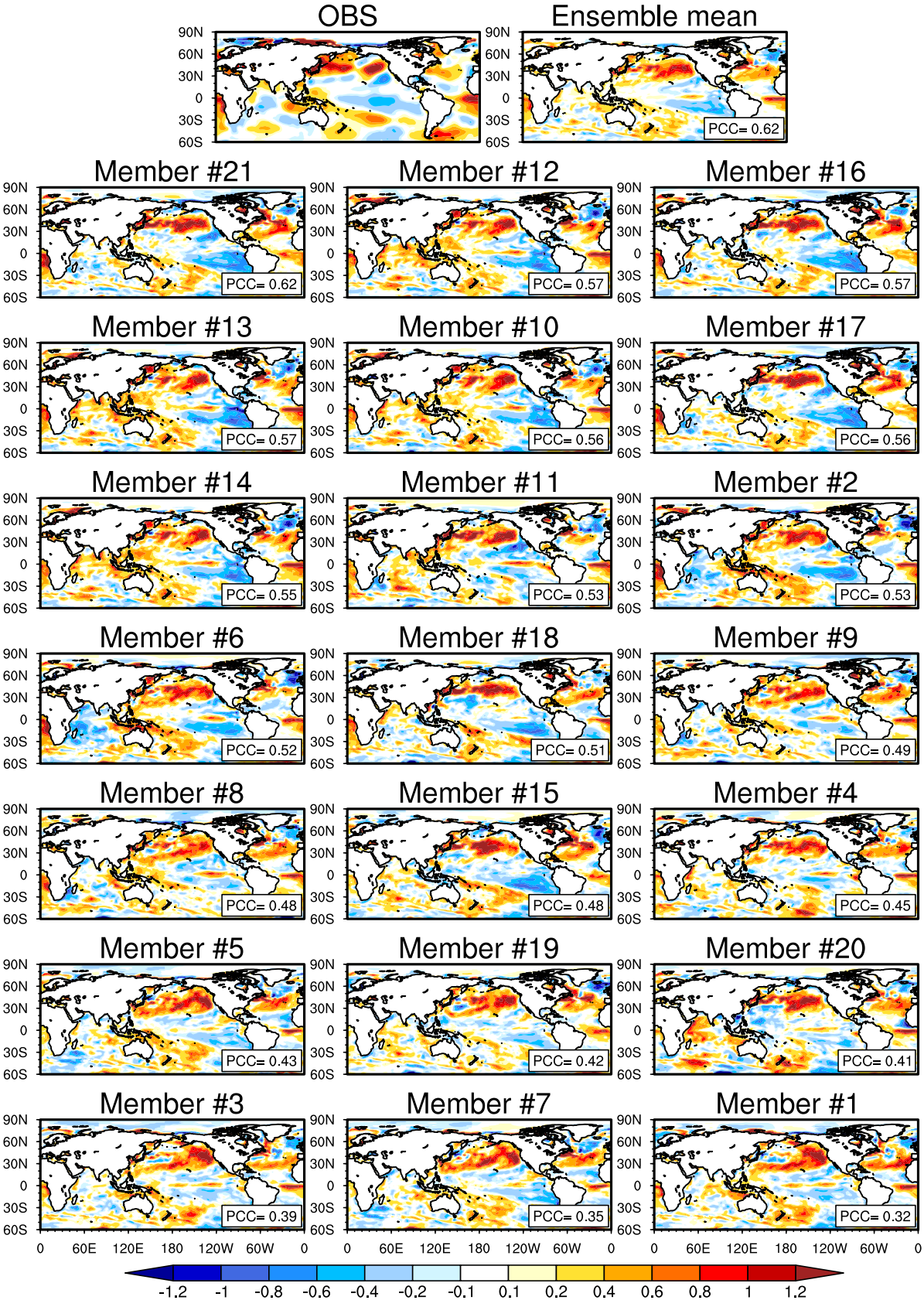

Fig. 6. Spatial distributions of the observed and predicted global SSTA (units: °C) in July 2021. The observation and ensemble mean forecast are shown on the left and the right of the first row. Forecasts from individual members are shown below the first row. PCC is the uncentered pattern correlation coefficient. The forecasts by the IAP-DecPreS are started from the end of June in 2021.

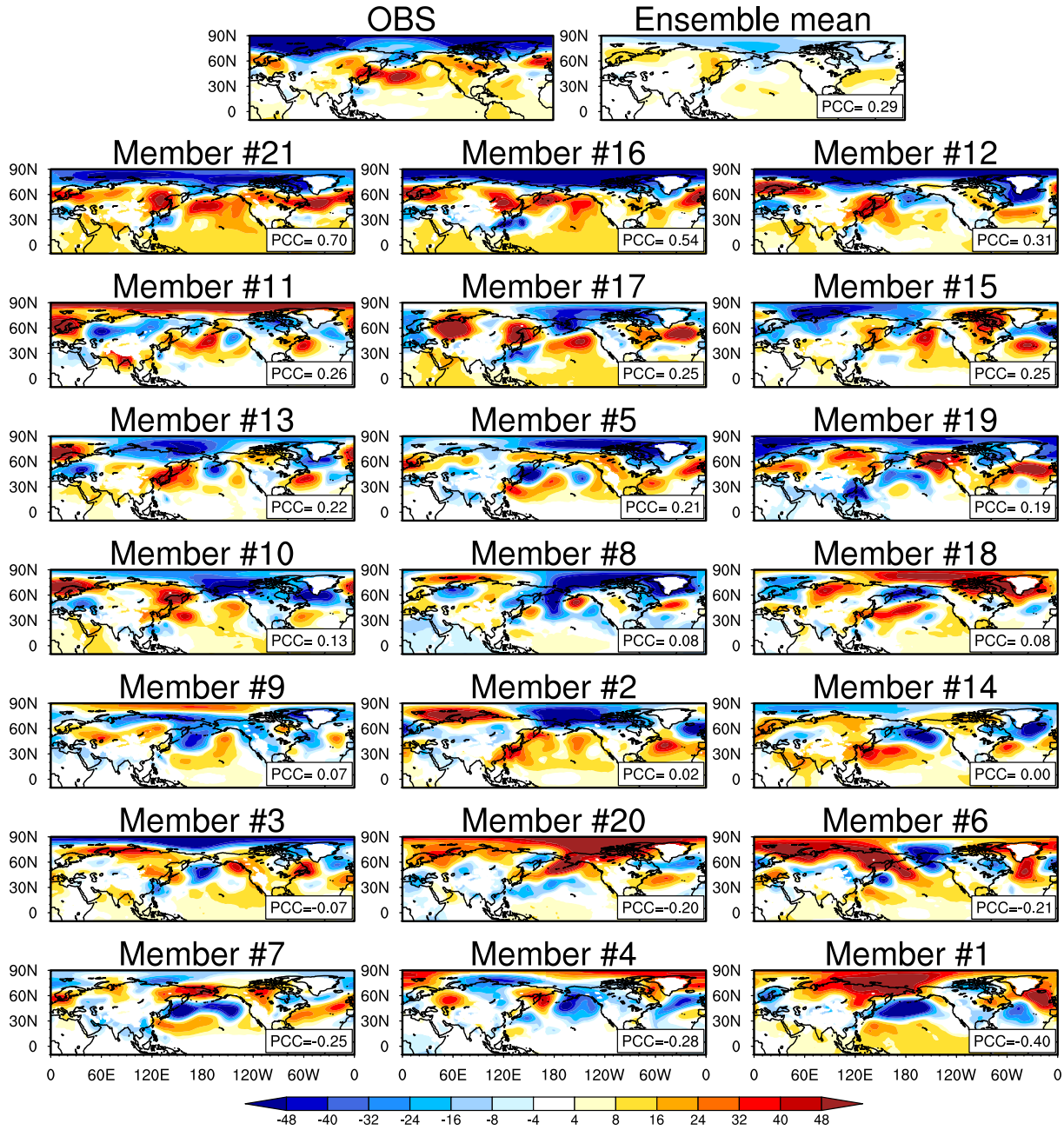

Fig. 7. As in Fig. 5, but for the 850-hPa geopotential height anomalies (units: gpm) over the Northern Hemisphere.

Table 2. The uncentered pattern correlation coefficient (PCC) between the forecasts and the observations for 850-hPa geopotential height field and SSTA in Figs. 6 and 7.

	PCC_{SST}	PCC_{Z850}		PCC_{SST}	PCC_{Z850}
Ens. Mean	0.62	0.29	Mem #11	0.53	0.26
Mem #1	0.32	−0.40	Mem #12	0.57	0.31
Mem #2	0.53	0.02	Mem #13	0.57	0.22
Mem #3	0.39	−0.07	Mem #14	0.55	0
Mem #4	0.45	−0.28	Mem #15	0.48	0.25
Mem #5	0.43	0.21	Mem #16	0.57	0.54
Mem #6	0.52	−0.21	Mem #17	0.56	0.25
Mem #7	0.35	−0.25	Mem #18	0.51	0.08
Mem #8	0.48	0.08	Mem #19	0.42	0.19
Mem #9	0.49	0.07	Mem #20	0.41	−0.20
Mem #10	0.56	0.13	Mem #21	0.62	0.70

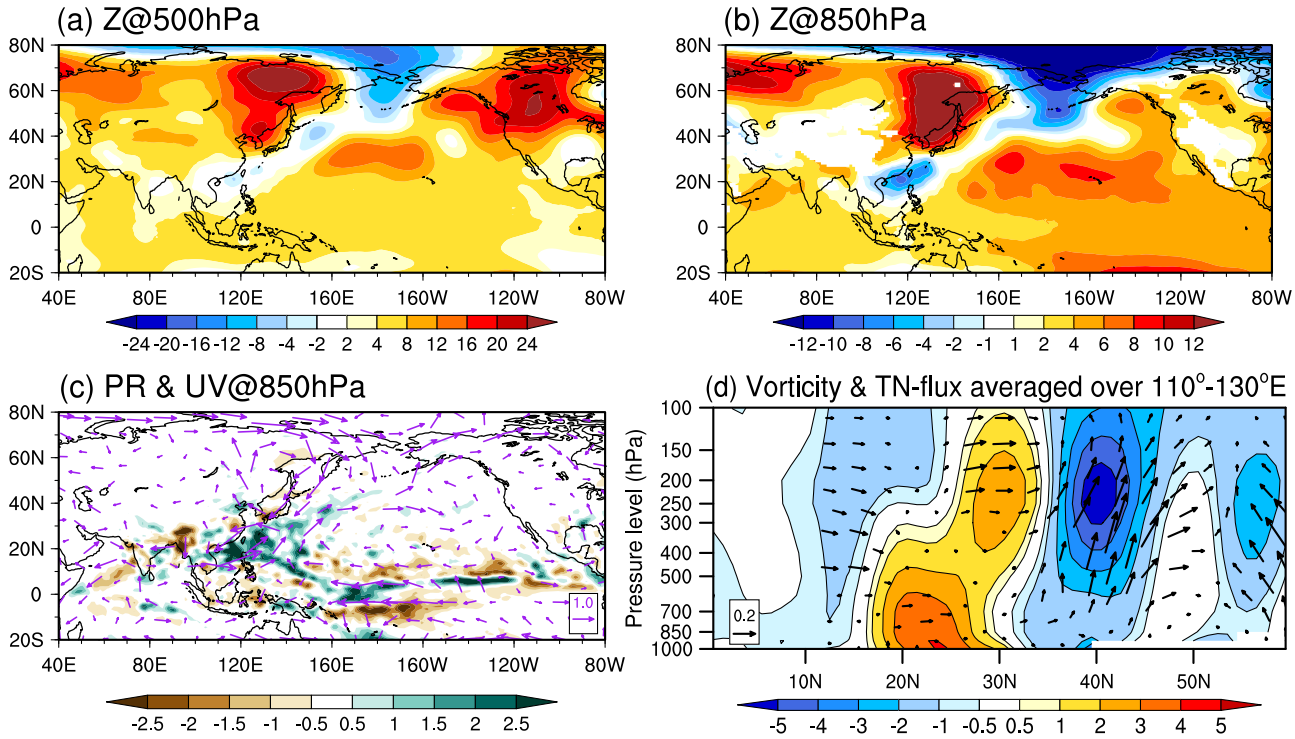

Fig. 8. The 21-member ensemble mean predicted (a) 500-hPa geopotential height anomalies (units: gpm), (b) 850-hPa geopotential height anomalies (units: gpm), (c) precipitation (shaded, units: mm d^{-1}) and 850-hPa horizontal wind (vector, units: m s^{-1}) anomalies, and (d) the meridional sections of relative vorticity (shaded, units: 10^{-6} s^{-1}) and TN-flux (vector, units: m^2 s^{-2}, the vertical components have been multiplied by 100) averaged between 110°–130°E in July 2021.

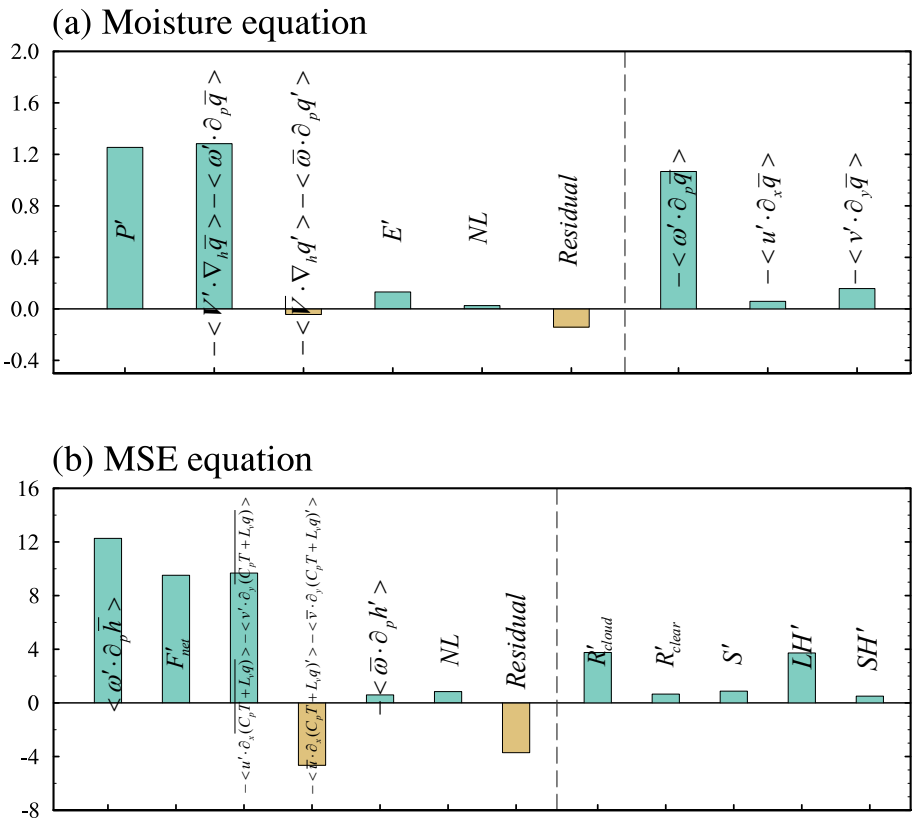

Fig. 9. Budget analysis for (a) the moisture equation [Eq. (1), units: mm d^{-1}] and (b) the MSE equation [Eqs. (4–5), units: W m^{-2}] for the area 10°–25°N, 125°–150°E in July 2021 from the 21-member ensemble mean forecasts by IAP-DecPreS.

150°E) indicated that the $<\omega'\partial_p\bar{h}>$ term is primarily balanced by positive net energy flux anomalies (F'_{net}) and the horizontal advection of climatological enthalpy by wind anomalies ($-<u'\partial_x\overline{(C_pT+L_vq)}>$ and $-<v'\partial_y\overline{(C_pT+L_vq)}>$), which represent two different physical processes.

The F'_{net} is determined by the cloud-related longwave radiative flux anomalies (R'_{cloud}) and the surface latent heat anomalies (LH′). The R'_{cloud} is generated by internal positive feedback between convection and cloud radiative forcing in the tropical atmosphere (Bretherton and Sobel, 2002; Su and Neelin, 2002; Neelin and Su, 2005). When the convection over the tropical western Pacific is enhanced, the deep convective clouds and associated cirrostratus and cirrocumulus will increase, which leads to a net warming of the atmospheric column, a further weakening of the gross moist stability of the atmospheric column, and thus an enhancement of the ascending flow and convective activities (Fig. 10a). The positive LH′ anomalies are associated with the strengthened

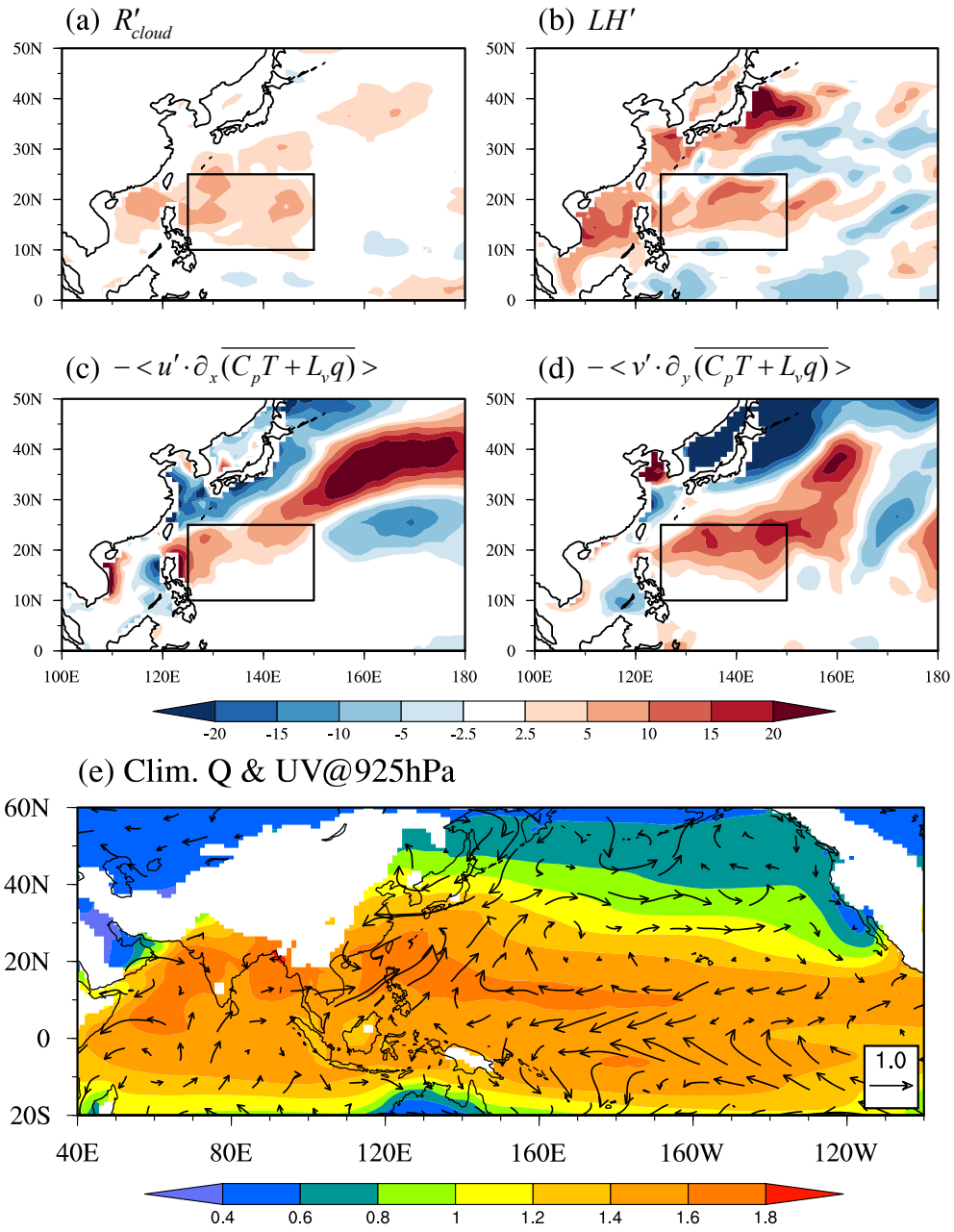

Fig. 10. Spatial distributions of (a) the cloud-related longwave radiative flux anomalies (R'_{cloud}), (b) the surface latent heat anomalies (LH′), (c) the zonal advection of climatological enthalpy by wind anomalies ($-<u'\partial_x\overline{(C_pT+L_vq)}>$), and (d) the meridianal advection of climatological enthalpy by wind anomalies ($-<v'\partial_y\overline{(C_pT+L_vq)}>$). (e) the July 925-hPa climatological specific humidity (shading; units: kg kg^{-1}) and 925-hPa horizontal wind anomalies in the 21-member ensemble mean predictions by IAP-DecPreS.

low-level summer monsoon circulations, which enhance surface evaporation and thus heat the atmospheric column and lead to ascending anomalies (Fig. 10b). The terms $-<u'\partial_x\overline{(C_pT+L_vq)}>$ and $-<v'\partial_y\overline{(C_pT+L_vq)}>$ are dominated by the anomalous horizontal advections of climatological latent heat energy by wind anomalies (Figs. 10c, d), which are more prominent at the low levels (not shown). At the 925-hPa level, the July climatological specific humidity over the tropical western Pacific is greater than the surroundings due to the outbreak of the western Pacific summer monsoon, which induces the positive meridional gradient of climatological specific humidity over the subtropical regions (Fig. 10e). The negative convective heating associated with the La Niña induces a pair of anomalous anticyclones over the tropical Pacific, one in both the Northern and Southern Hemisphere. There are southwesterlies at the west edge of the northern anticyclone, which strengthen the monsoonal circulations and induce the positive moisture enthalpy advection anomalies over the tropical western Pacific (Fig. 10e).

The above analysis demonstrates that the predictable component of the northward shift of the WPSH is related to the PJ pattern, which originates from the tropical circulation anomalies associated with the La Niña event and associated local positive cloud–radiation and wind–SST–evaporation feedbacks.

4.2. *Unpredictable variability*

The predictable component only contributes 28.0% of the observed WPSH variation in July 2021, and thus, the remaining 72.0% of the variation is associated with the unpredictable component. The leading modes of the unpredictable variability of the circulation anomalies are obtained by performing EOF analysis on the ensemble spread of the 500-hPa geopotential height anomalies over northeastern East Asia (20°–60°N, 110°–170°E). The first two EOF modes account for 49.5% and 17.4% of the total variance, respectively. The first EOF (EOF1) shows a meridional tripole pattern of geopotential height anomalies over the coastal regions of East Asia, with negative anomalies over the northern part of the Philippine Sea and the Bering Strait and positive anomalies over the northern part of Japan (Fig. 11a). The second EOF (EOF2) exhibits more prominent geopotential anomalies over the midlatitude to high-latitude regions, with weak positive anomalies to the east of Japan (Fig. 11b). Relationships between the normalized principal components corresponding to the first two EOF modes (PC1 and PC2) and the ensemble spread of the Z850 dipole index are shown in Figs. 11b and d. The predicted Z850 dipole index in the ensemble members ranges from –53.4 gpm to 62.2 gpm, which covers the

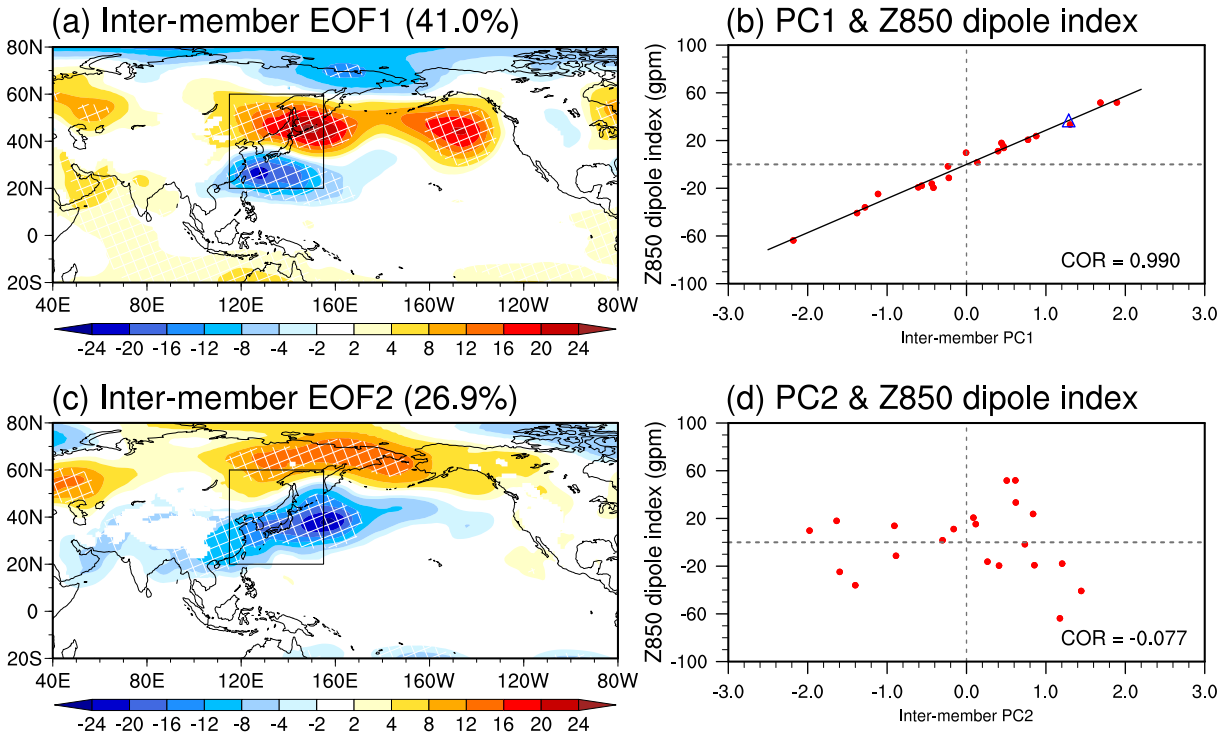

Fig. 11. Spatial distributions of the 850-hPa geopotential height anomalies (units: gpm) associated with (a) the first EOF mode (EOF1) and (c) the second EOF mode (EOF2) of the ensemble spread of the forecasts. Variance contributions of the two EOF modes are noted in the parentheses. Relationships between predicted Z850 dipole index and (b) the normalized principal component (PC) corresponding to the first EOF mode (PC1) and (d) the normalized PC corresponding to the second EOF mode (PC2). The correlation coefficients between PC1 (PC2) and the predicted Z850 dipole index are shown in the legends. The black line in (b) is the linear fitting equation between PC1 and the predicted Z850 dipole index. The blue triangle represents the observation, for which the PC value is estimated through the linear fitting equation in the model world. The hatching in (a, c) denotes values exceeding the 95% confidence level.

observed value of 36.8 pgm. EOF1 has a closer correlation relationship with the original prediction than EOF2, with the correlation coefficient reaching 0.99 (significant at the 99% level). The agreement between the observed Z850 dipole index and the predictions in the members with greater loading of EOF1 indicates that the combination of the predictable component and the extreme positive phase of EOF1 can reproduce the observed northward shift of the WPSH in July 2021. The low correlation coefficient between PC2 and the ensemble spread of the Z850 dipole index indicates that EOF2 is not the main factor dominating the unpredictable variability (Fig. 11d), and we further verify that EOF2 is associated with the midlatitude wave train over Eurasia (not shown). In the following analysis, we focus on the formation mechanism of EOF1.

The circulation, precipitation, and SST anomalies associated with EOF1 are shown in Fig. 12. EOF1 exhibits a typical PJ pattern, with the upper-level circulation anomalies shifted meridionally relative to the low-level anomalies by about a quarter wavelength and northward (southeastward) propagation of the Rossby waves in the lower (upper) troposphere (Figs. 12a, c, e). There are no significant SSTAs associated with EOF1 except for those in the northern Pacific, which are below the centers of the PJ pattern-related anomalous atmospheric activity (Fig. 12b), indicating that EOF1 is independent of the SSTA's forcing. The PJ pattern of EOF1 is closely related to the monthly precipitation anomalies over the tropical western Pacific (Fig. 12d), which was suggested to be internally generated by both the intraseasonal and synoptic variabilities (Kawamura and Ogasawara, 2006;

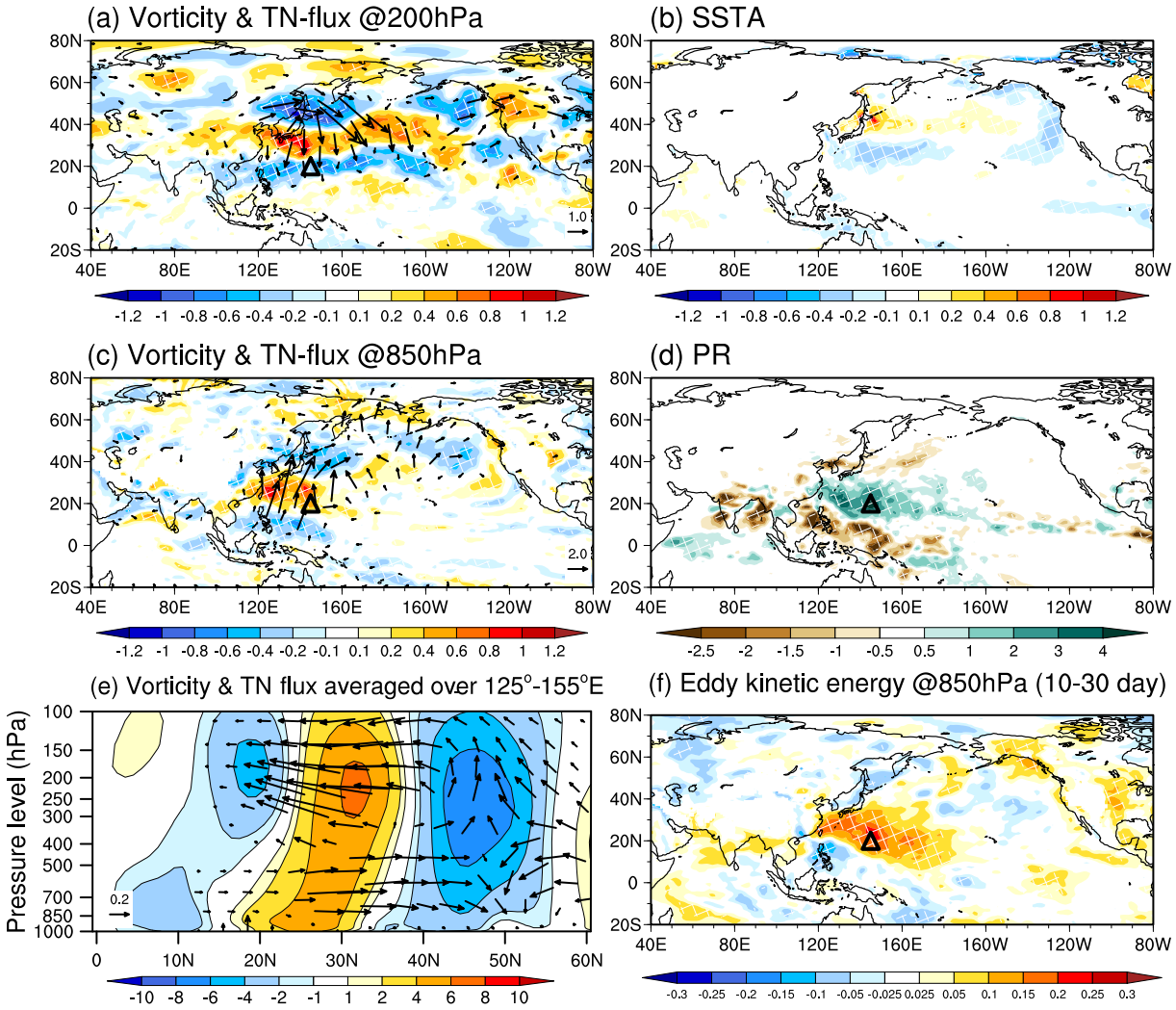

Fig. 12. Regressions of the ensemble spread of (a) relative vorticity (shaded; units: $m^2\ s^{-2}$) and TN-flux (vector, units: $m^2\ s^{-2}$) anomalies at 200 hPa, (b) SSTA (units: °C), (c) relative vorticity (shaded; units: $m^2\ s^{-2}$) and TN-flux (vector, units: $m^2\ s^{-2}$) anomalies at 850 hPa, (d) precipitation anomalies (units: mm d^{-1}), (e) the meridional sections of relative vorticity (shaded, units: $10^{-6}\ s^{-1}$) and TN-flux (vector, units: $m^2\ s^{-2}$, the vertical components have been multiplied by 100) averaged between 110°–130°E, and (f) 850-hPa eddy kinetic energy (units: $m^2\ s^{-2}$) at a time scale of 10–30 days onto the normalized principal component (PC) corresponding to the first EOF mode (PC1) of the ensemble spread of the forecasts in July 2021. The hatching denotes values exceeding the 95% confidence level. The triangles in (a, c, d, f) represent the center of precipitation anomaly over the western tropical Pacific.

Yamada and Kawamura, 2007; Wang et al., 2016).

To determine what kind of internal variability induces the EOF1-related precipitation anomalies over the tropical western Pacific, we diagnosed the column-integrated atmospheric moisture equation at intraseasonal (10–30 d) and synoptic (<10 d) time scales based on the daily data. The moisture budget associated with EOF1 indicates that the precipitation anomalies over the tropical western Pacific at the monthly time scale are dominated by the intraseasonal variability (Fig. 13). This is further confirmed by the significant 850-hPa eddy kinetic energy at a time scale of 10–30 days over the tropical western Pacific associated with EOF1 (Fig. 12f). Hence, different from the La Niña-forced PJ pattern, the PJ pattern related to EOF1 here is generated by the atmospheric internal processes due to intraseasonal variability.

5. Conclusion and discussion

One of the dominant atmospheric circulation systems accompanying the unprecedented Zhengzhou extreme rainfall in July 2021 was the northward shift of the WPSH. The predictability of the anomalous WPSH activity is investigated by combining observational analysis with ensemble seasonal prediction hindcast experiments using the IAP-DecPreS climate prediction system. Both the predictable and unpredictable components of the WPSH variability are identified with physical mechanisms being clarified. The main conclusions are summarized below.

1) The observational analysis reveals that the large-scale atmospheric circulation anomalies associated with the Zhengzhou extreme rainfall in July 2021 are part of the northward shift of the WPSH, which is the strongest observed since the 1979. The intensity of the northward shift of the WPSH cannot be solely explained by the concurrent weak La Niña event and is closely related to the convection activity over the tropical western Pacific, which modulates the WPSH via exciting the PJ pattern. The specific PJ pattern in July 2021 has a larger intensity and shifts northward, which is responsible for the abnormal northward shift of the WPSH in July 2021.

2) The predictability of the northward shift of the WPSH in July 2021 is examined by using 21-member 3-month ensemble seasonal predictions using the IAP-DecPreS climate prediction system. The ensemble mean reasonably predicts the positive 850-hPa geopotential height anomalies over the midlatitude Far East, but the intensity is weaker than that seen in the observations. The predictions from two ensemble members closely match the observations

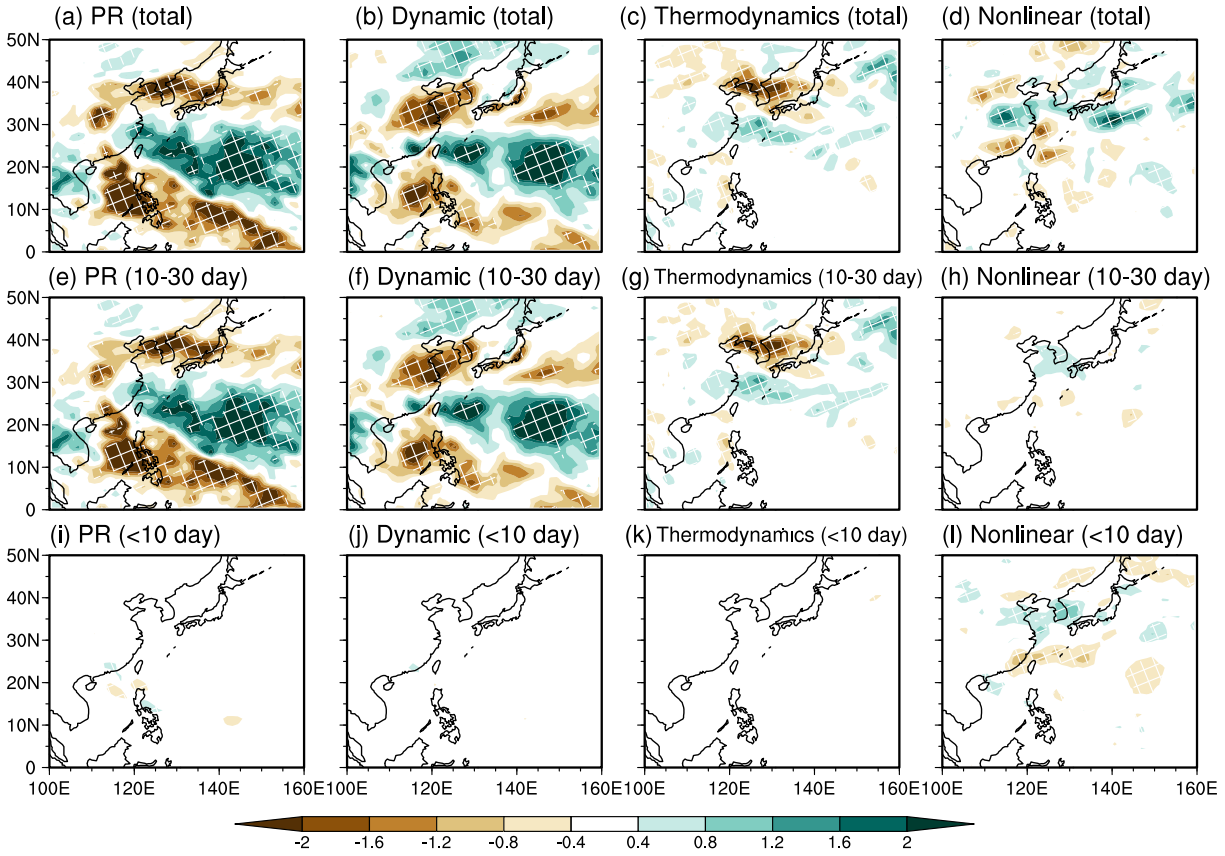

Fig. 13. Regressions of the ensemble spread of moisture budgets onto the normalized principal component (PC) corresponding to the first EOF mode (PC1) of the ensemble spread of the forecasts in July 2021 at time scales of (a–d) monthly, (e–h) 10–30 days, and (i–l) less than 10 days. (a, e, i) precipitation anomalies and (b, f, j) the dynamic components, (c, g, k) the thermodynamic components, and (d, h, l) the nonlinear components of the anomalous moisture advection. The hatching denotes values exceeding the 95% confidence level.

in the context of both the spatial pattern and intensity. The relative contribution of the predictable and unpredictable components to the observed WPSH variation in July 2021 are 28.0% and 72.0%, respectively.

3) Both the predictable and unpredictable components of the WPSH variation are identified by analyzing ensemble predictions. The predictable component stems from the predictable positive precipitation anomalies over the tropical western Pacific. These positive precipitation anomalies are induced by the tropical anticyclonic anomalies associated with the La Niña-related negative convective heating anomalies over the tropical Pacific. The southwesterlies at the western edge of the anomalous anticyclone induce positive anomalous advection of climatological moisture enthalpy into the tropical western Pacific and strengthen the low-level summer monsoon circulations and local evaporation; both processes enhance the atmospheric MSE and, thus, drive anomalous ascending motion to strengthen the precipitation. The unpredictable component is the PJ pattern generated by the atmospheric internal intraseasonal oscillations. The superposition of the predictable variabilities and the positive phase of the internally generated PJ pattern can reproduce the observed northward shift of the WPSH in July 2021.

There are two implications of this study. The first is for studies based on observational data; the contribution of intraseasonal variability over the western tropical Pacific to the observed northward shift of the WPSH in July 2021 deserves further attention. The second implication is for the further development of the IAP-DecPreS; an accurate prediction of the intraseasonal variability should be of high priority in the efforts devoted to improving the prediction skill of East Asian summer climate. In addition to the prediction of large-scale circulation at both seasonal and intraseasonal time scales, an accurate prediction of such extremes also needs to consider the impact of Typhoon "In-Fa" (2021) and local processes at the synoptic time scale. We hope that the development of Convection Permitting Models (CPMs) will help us to increase the prediction skill. As a final note, this study is based on 21-member seasonal forecast experiments using a single model. Possible model dependence of the results and incomplete isolation between predictable and unpredictable variabilities due to limited ensemble members deserves further assessment by using large ensemble seasonal forecast experiments of multiple models.

Acknowledgements. This work is supported by the National Natural Science Foundation of China under Grant No. 41988101, the Chinese Academy of Sciences under Grant XDA20060102, the China Postdoctoral Science Foundation under Grant No. 2022T150638 and K. C. Wong Education Foundation.

REFERENCES

Back, L. E., and C. S. Bretherton, 2006: Geographic variability in the export of moist static energy and vertical motion profiles in the tropical Pacific. *Geophys. Res. Lett.*, **33**, L17810, https://doi.org/10.1029/2006gl026672.

Biasutti, M., and Coauthors, 2018: Global energetics and local physics as drivers of past, present and future monsoons. *Nature Geoscience*, **11**, 392–400, https://doi.org/10.1038/s41561-018-0137-1.

Boer, G. J., and Coauthors, 2016: The decadal climate prediction project (DCPP) contribution to CMIP6. *Geoscientific Model Development*, **9**, 3751–3777, https://doi.org/10.5194/gmd-9-3751-2016.

Boer, G. J., W. J. Merryfield, and V. V. Kharin, 2018: Relationships between potential, attainable, and actual skill in a decadal prediction experiment. *Climate Dyn.*, **52**, 4813–4831, https://doi.org/10.1007/s00382-018-4417-7.

Bretherton, C. S., and A. H. Sobel, 2002: A simple model of a convectively-coupled Walker circulation using the weak temperature gradient approximation. *J. Climate*, **15**, 2907–2920, https://doi.org/10.1175/1520-0442(2002)015,2907:ASMOAC.2.0.CO;2.

Chen, X. L., and T. J. Zhou, 2014: Relative role of tropical SST forcing in the 1990s periodicity change of the Pacific-Japan pattern interannual variability. *J. Geophys. Res.*, **119**, 13 043–13 066, https://doi.org/10.1002/2014jd022064.

Cheng, J. B., Y. H. Zhao, R. Zhi, and G. L. Feng, 2022: Analysis of the July 2021 extreme precipitation in Henan using the novel moisture budget equation. *Theor. Appl. Climatol.*, **149**, 15–24, https://doi.org/10.1007/s00704-022-04022-7.

Chou, C. A., J. C. H. Chiang, C. W. Lan, C. H. Chung, Y. C. Liao, and C. J. Lee, 2013: Increase in the range between wet and dry season precipitation. *Nature Geoscience*, **6**, 263–267, https://doi.org/10.1038/ngeo1744.

Gill, A. E., 1980: Some simple solutions for heat-induced tropical circulation. *Quart. J. Roy. Meteor. Soc.*, **106**, 447–462, https://doi.org/10.1002/qj.49710644905.

Good, S. A., M. J. Martin, and N. A. Rayner, 2013: EN4: Quality controlled ocean temperature and salinity profiles and monthly objective analyses with uncertainty estimates. *J. Geophys. Res.*, **118**, 6704–6716, https://doi.org/10.1002/2013jc009067.

Guo, Y., Y. Q. Yu, P. F. Lin, H. L. Liu, B. He, Q. Bao, S. W. Zhao, and X. W. Wang, 2020a: Overview of the CMIP6 historical experiment datasets with the climate system model CAS FGOALS-f3-L. *Adv. Atmos. Sci.*, **37**, 1057–1066, https://doi.org/10.1007/s00376-020-2004-4.

Guo, Y. Y., and Coauthors, 2020b: Simulation and improvements of oceanic circulation and sea ice by the coupled climate system model FGOALS-f3-L. *Adv. Atmos. Sci.*, **37**, 1133–1148, https://doi.org/10.1007/s00376-020-0006-x.

He, B., and Coauthors, 2020a: CAS FGOALS-f3-L model datasets for CMIP6 GMMIP tier-1 and Tier-3 experiments. *Adv. Atmos. Sci.*, **37**, 18–28, https://doi.org/10.1007/s00376-019-9085-y.

He, B., and Coauthors, 2020b: CAS FGOALS-f3-L model dataset descriptions for CMIP6 DECK experiments. *Atmos. Ocean. Sci. Lett.*, **13**, 582–588, https://doi.org/10.1080/16742834.2020.1778419.

Hersbach, H., and Coauthors, 2020: The ERA5 global reanalysis. *Quart. J. Roy. Meteor. Soc.*, **146**, 1999–2049, https://doi.org/10.1002/qj.3803.

Hu, S., B. Wu, T. J. Zhou, and Z. Guo, 2019: A comparison of full-field and anomaly initialization for seasonal prediction of Indian Ocean basin mode. *Climate Dyn.*, **53**, 6089–6104, https://doi.org/10.1007/s00382-019-04916-9.

Hu, S., T. J. Zhou, and B. Wu, 2020: Improved ENSO prediction

skill resulting from reduced climate drift in IAP-DecPreS: A comparison of full-field and anomaly initializations. *Journal of Advances in Modeling Earth Systems*, **12**, e2019MS001759, https://doi.org/10.1029/2019ms001759.

Huang, R. H., and F. Y. Sun, 1992: Impacts of the tropical western Pacific on the East Asian summer monsoon. *J. Meteor. Soc. Japan*, **70**, 243–256, https://doi.org/10.2151/jmsj1965.70.1B_243.

Kawamura, R., and T. Ogasawara, 2006: On the role of typhoons in generating PJ teleconnection patterns over the western North Pacific in late summer. *SOLA*, **2**, 37–40, https://doi.org/10.2151/sola.2006-010. https://doi.org/10.2151/sola.2006-010.

Kosaka, Y., and H. Nakamura, 2006: Structure and dynamics of the summertime Pacific–Japan teleconnection pattern. *Quart. J. Roy. Meteor. Soc.*, **132**, 2009–2030, https://doi.org/10.1256/qj.05.204.

Kosaka, Y., and H. Nakamura, 2010: Mechanisms of meridional teleconnection observed between a summer monsoon system and a subtropical anticyclone. Part I: The Pacific–Japan Pattern. *J. Climate*, **23**, 5085–5108, https://doi.org/10.1175/2010jcli3413.1.

Kubota, H., Y. Kosaka, and S. P. Xie, 2016: A 117-year long index of the Pacific-Japan pattern with application to interdecadal variability. *International Journal of Climatology*, **36**, 1575–1589, https://doi.org/10.1002/joc.4441.

Lau, K. M., and H. Weng, 2002: Recurrent Teleconnection Patterns Linking Summertime Precipitation Variability over East Asia and North America. *Journal of the Meteorological Society of Japan. Ser. II*, **80**(6), 1309-1324, https://doi.org/10.2151/jmsj.80.1309.

Li, J. X., Q. Bao, Y. M. Liu, G. X. Wu, L. Wang, B. He, X. C. Wang, and J. D. Li, 2019: Evaluation of FAMIL2 in simulating the climatology and seasonal-to-Interannual variability of tropical cyclone characteristics. *Journal of Advances in Modeling Earth Systems*, **11**, 1117–1136, https://doi.org/ 10.1029/2018MS001506. https://doi.org/10.1029/2018MS001506.

Liang, X. D., and Coauthors, 2022: Preliminary investigation on the extreme rainfall event during July 2021 in Henan Province and its multi-scale processes. *Chinese Science Bulletin*, **67**, 997–1011, https://doi.org/10.1360/tb-2021-0827.

Lin, P. F., and Coauthors, 2020: LICOM model datasets for the CMIP6 ocean model intercomparison project. *Adv. Atmos. Sci.*, **37**, 239–249, https://doi.org/10.1007/s00376-019-9208-5.

Ling, S. N., and R. Y. Lu, 2022: Tropical cyclones over the western north pacific strengthen the East Asia—Pacific pattern during summer. *Adv. Atmos. Sci.*, **39**, 249–259, https://doi.org/10.1007/s00376-021-1171-2.

Neelin, J. D., and I. M. Held, 1987: Modeling tropical convergence based on the moist static energy budget. *Mon. Wea. Rev.*, **115**, 3–12, https://doi.org/10.1175/1520-0493(1987)115<0003:mtcbot>2.0.co;2.

Neelin, J. D., and H. Su, 2005: Moist teleconnection mechanisms for the tropical South American and Atlantic sector. *J. Climate*, **18**, 3928–3950, https://doi.org/10.1175/JCLI3517.1.

Nie, Y. B., and J. Q. Sun, 2022: Moisture sources and transport for extreme precipitation over Henan in July 2021. *Geophys. Res. Lett.*, **49**, e2021GL097446, https://doi.org/10.1029/2021gl097446.

Nitta, T., 1987: Convective activities in the tropical western pacific and their impact on the northern hemisphere summer circulation. *J. Meteor. Soc. Japan*, **65**, 373–390, https://doi.org/10.2151/jmsj1965.65.3_373.

Rayner, N. A., D. E. Parker, E. B. Horton, C. K. Folland, L. V. Alexander, D. P. Rowell, E. C. Kent, and A. Kaplan, 2003: Global analyses of sea surface temperature, sea ice, and night marine air temperature since the late nineteenth century. *J. Geophys. Res.*, **108**, 4407, https://doi.org/10.1029/2002jd002670.

Seager, R., N. Naik, and G. A. Vecchi, 2010: Thermodynamic and dynamic mechanisms for large-scale changes in the hydrological cycle in response to global warming. *J. Climate*, **23**, 4651–4668, https://doi.org/10.1175/2010jcli3655.1.

Seager, R., N. Naik, and L. Vogel, 2012: Does global warming cause intensified interannual hydroclimate variability? *J. Climate*, **25**, 3355–3372, https://doi.org/10.1175/jcli-d-11-00363.1.

Sun, Y. X., G. Chen, and B. K. Tan, 2021: Formation and maintenance mechanisms of the Pacific-Japan pattern as an intraseasonal variability mode. *Climate Dyn.*, **57**, 2971–2994, https://doi.org/10.1007/s00382-021-05851-4.

Su, H., and J. D. Neelin, 2002: Teleconnection mechanism for tropical Pacific descent anomalies during El Niño. *J. Atmos. Sci.*, **59**, 2694–2712, https://doi.org/10.1175/1520-0469(2002)059,2694:TMFTPD.2.0.CO;2.

Takaya, K., and H. Nakamura, 2001: A formulation of a phase-independent wave-activity flux for stationary and migratory quasigeostrophic eddies on a zonally varying basic flow. *J. Atmos. Sci.*, **58**, 608–627, https://doi.org/10.1175/1520-0469(2001)058<0608:Afoapi>2.0.Co;2.

Takemura, K., and H. Mukougawa, 2020: Dynamical relationship between quasi-stationary rossby wave propagation along the Asian Jet and Pacific-Japan Pattern in boreal summer. *J. Meteor. Soc. Japan*, **98**, 169–187, https://doi.org/10.2151/jmsj.2020-010.

Tao, L., T. M. Li, Y. H. Ke, and J. W. Zhao, 2017: Causes of interannual and interdecadal variations of the summertime Pacific-Japan-like pattern over East Asia. *J. Climate*, **30**, 8845–8864, https://doi.org/10.1175/jcli-d-15-0817.1.

Tao, S. Y., and L. X. Chen, 1987: A review of recent research of the east Asian summer monsoon in China. *Monsoon Meteorology*. Vol. 7, *Oxford Monogr. Geol. Geophys.*, C.-P. Chang and T. N. Krishnamurti, Eds., Oxford Univ. Press, New York, 60–92.

Wang, J. B., Z. P. Wen, R. G. Wu, Y. Y. Guo, and Z. S. Chen, 2016: The mechanism of growth of the low-frequency East Asia–Pacific teleconnection and the triggering role of tropical intraseasonal oscillation. *Climate Dyn.*, **46**, 3965–3977, https://doi.org/10.1007/s00382-015-2815-7.

Wu, B., and T. J. Zhou, 2008: Oceanic origin of the interannual and interdecadal variability of the summertime western Pacific subtropical high. *Geophys. Res. Lett.*, **35**, L13701, https://doi.org/10.1029/2008gl034584.

Wu, B., X. L. Chen, F. F. Song, Y. Sun, and T. J. Zhou, 2015: Initialized decadal predictions by LASG/IAP climate system model FGOALS-s2: Evaluations of strengths and weaknesses. *Advances in Meteorology*, **2015**, 904826, https://doi.org/10.1155/2015/904826.

Wu, B., T. J. Zhou, and T. M. Li, 2016: Impacts of the Pacific–Japan and circumglobal teleconnection patterns on the interdecadal variability of the East Asian Summer monsoon. *J. Climate*, **29**, 3253–3271, https://doi.org/10.1175/jcli-d-15-0105.1.

Wu, B., T. J. Zhou, and T. Li, 2017: Atmospheric dynamic and thermodynamic processes driving the western North Pacific anomalous anticyclone during El Niño. Part I: Maintenance mechanisms. *J. Climate*, **30**, 9621–9635, https://doi.org/10.1175/jcli-d-16-0489.1.

Wu, B., T. J. Zhou, and F. Zheng, 2018: EnOI-IAU initialization scheme designed for decadal climate prediction system IAP-DecPreS. *Journal of Advances in Modeling Earth Systems*, **10**, 342–356, https://doi.org/10.1002/2017ms001132.

Xiang, B. Q., B. Wang, W. D. Yu, and S. B. Xu, 2013: How can anomalous western North Pacific Subtropical High intensify in late summer. *Geophys. Res. Lett.*, **40**, 2349–2354, https://doi.org/10.1002/grl.50431.

Xu, P. Q., L. Wang, W. Chen, J. Feng, and Y. Y. Liu, 2019: Structural changes in the Pacific-Japan Pattern in the late 1990s. *J. Climate*, **32**, 607–621, https://doi.org/10.1175/jcli-d-18-0123.1.

Yamada, K., and R. Kawamura, 2007: Dynamical link between typhoon activity and the PJ teleconnection pattern from early summer to autumn as revealed by the JRA-25 reanalysis. *Sola*, **3**, 65–68, https://doi.org/10.2151/sola.2007-017.

Yang, W. T., F. Gao, T. H. Xu, N. Z. Wang, J. S. Tu, L. L. Jing, and Y. H. Kong, 2021: Daily flood monitoring based on spaceborne GNSS-R data: A case study on Henan, China. *Remote Sensing*, **13**, 4561, https://doi.org/10.3390/rs13224561.

Yu, Y. Q., S. L. Tang, H. L. Liu, P. F. Lin, and X. L. Li, 2018: Development and evaluation of the dynamic framework of an ocean general circulation model with arbitrary orthogonal curvilinear coordinate. *Chinese Journal of Atmospheric Sciences*, **42**, 877–889, https://doi.org/10.3878/j.issn.1006-9895.1805.17284. (in Chinese with English abstract)

Zhang, S. C., and Coauthors, 2021: Using CYGNSS data to map flood inundation during the 2021 extreme precipitation in Henan Province, China. *Remote Sensing*, **13**, 5181, https://doi.org/10.3390/rs13245181.

Zhang, S. H., Y. R. X. Chen, Y. L. Luo, B. Liu, G. Y. Ren, T. J. Zhou, C. Martinez - villalobos, and M. Y. Chang, 2022: Revealing the circulation pattern most conducive to precipitation extremes in Henan Province of North China. *Geophys. Res. Lett.*, **49**, e2022GL098034, https://doi.org/10.1029/2022gl098034.

Zhou, L. J., and Coauthors, 2015: Global energy and water balance: Characteristics from Finite-volume Atmospheric Model of the IAP/LASG (FAMIL1). *Journal of Advances in Modeling Earth Systems*, **7**, 1–20, https://doi.org/10.1002/2014MS000349.

Zhou, T. J., and Coauthors, 2020: Development of climate and earth system models in China: Past achievements and new CMIP6 results. *J. Meteor. Res.*, **34**, 1–19, https://doi.org/10.1007/s13351-020-9164-0.

Zhou, T. J., and Coauthors, 2022: 2021: A year of unprecedented climate extremes in eastern Asia, North America, and Europe. *Adv. Atmos. Sci.*, **39**, 1598–1607, https://doi.org/10.1007/s00376-022-2063-9.

Zhu, Z. W., and T. Li, 2016: A new paradigm for continental U.S. summer rainfall variability: Asia–North America teleconnection. *J. Climate*, **29**, 7313–7327, https://doi.org/10.1175/jcli-d-16-0137.1.

Zhu, Z. W., and T. Li, 2018: Amplified contiguous United States summer rainfall variability induced by East Asian monsoon interdecadal change. *Climate Dyn.*, **50**, 3523–3536, https://doi.org/10.1007/s00382-017-3821-8.